# Revisiting Winter Arctic Ice Mass Balance Observations With a 1-D Model: Sensitivity Studies, Snow Density Estimation, Flooding, and Snow Ice Formation

Sarah Gani, Jérôme Sirven, Nathalie Sennéchael, Christine Provost

JGR Oceans

RESEARCH ARTICLE
10.1029/2019JC015431

# Revisiting Winter Arctic Ice Mass Balance Observations With a 1-D Model: Sensitivity Studies, Snow Density Estimation, Flooding, and Snow Ice Formation

**Sarah Gani[1], Jérôme Sirven[1], Nathalie Sennéchael[1], and Christine Provost[1]**

[1]IPSL/LOCEAN/UPMC/CNRS/IRD/MNHN, Sorbonne Université, Paris, France

**Key Points:**
- We revisited winter ice mass balance observations, using 1-D simulations of snow and ice temperature profiles
- We combined observations and 1-D modelling to adjust the snow density profiles, which are crucial for simulating sea ice evolution
- The simulations provided accurate temperature profiles and an estimation of ice salinity and brine fraction evolution during flooding

**Correspondence to:**
S. Gani,
sarah.gani@locean-ipsl.upmc.fr

**Citation:**
Gani, S., Sirven, J., Sennéchael, N., & Provost, C. (2019). Revisiting winter arctic ice mass balance observations with a 1-D model: Sensitivity studies, snow density estimation, flooding, and snow ice formation.. *Journal of Geophysical Research: Oceans*, *124*. https://doi.org/10.1029/2019JC015431

Received 28 JUN 2019
Accepted 23 NOV 2019
Accepted article online 30 NOV 2019

**Abstract** We used a state-of-the art one-dimensional snow and ice model (the LIM1D model), to simulate data collected in winter 2015 north of Svalbard with ice mass balance instruments. The quality of the simulations was assessed by comparing simulated temperature profiles and sea ice thicknesses with the data: The root-mean-square difference between observed and modeled temperature was 1.06 °C in snow and 0.19 °C in ice, and the root-mean-square difference between simulated and observed ice thickness was 2.0 cm (snow depth was prescribed). The long-wave heat flux from the ERA-I reanalysis was adequate to perform winter numerical simulations; in contrast, the ERA-I air temperature induced large errors in the snow and ice temperature. Snow density had a direct impact on heat transfers and, thus, on the simulation. The joint use of the data and the simulations permitted the adjustment of the snow density profiles with a light (240 kg/m$^3$) snow deposited on top of a denser (370 kg/m$^3$) snow. The ice flooding, which occurred after a storm-induced breakup of floes loaded with snow, was simulated by prescribing the observed lower limit of the snow. The simulations provided insights on the evolution of sea ice bulk salinity, brine fraction, and the amount of snow ice formed during the flooding event.

**Plain Language Summary** A state-of-the-art snow and ice model (the model LIM1D) was used to simulate observations collected in winter 2015 north of Svalbard. The model estimated sea ice bulk salinity and brine fraction, which cannot be measured continuously. Combining observations and 1-D modeling allowed adjustments of the snow density (and conductivity) profiles, which have a critical impact on the simulation.

## 1. Introduction

During the past few decades, the Arctic sea ice regime has undergone large changes resulting in a smaller, thinner, and faster-moving ice cover (Lindsay & Schweiger, 2015; Spreen et al., 2011). The key role of sea ice in the global climate system motivated the development of thermodynamic and dynamic models to understand and forecast its evolution. Despite advances in numerical modeling, the reliability of present-day climate prediction models is limited in the Arctic and projected rates of sea ice decline remain uncertain (Overland & Wang, 2013). Several studies have investigated the sensitivity of sea ice thickness and area to model parameters and oceanic and atmospheric forcing. Sea ice thickness and extent were found to be most sensitive to ice density, albedo, and emissivity in summer and to the snow density, atmospheric and oceanic forcing in winter (Kim et al., 2006; Urrego-Blanco et al., 2016).

Small-scale physical processes that play an important role in the Arctic atmosphere/snow/sea ice/ocean system, in particular at the interfaces, are still not well represented in climate models (Vihma et al., 2014). One-dimensional sea ice models can help improve this situation. They provide efficient tools for developing and testing parameterizations of physical and biogeochemical processes within sea ice and snow and for interpreting field observations (Vancoppenolle & Tedesco, 2017). One-dimensional models may help to interpret the data collected with ice mass balance instruments and provide complementary information on parameters that cannot be measured continuously. Huwald et al. (2005) developed a multilayer sigma-coordinate thermodynamic sea ice model and compared simulations to the observational data from the Surface Heat Budget of the Arctic Ocean experiment (Persson et al., 2002). When the initial ice thickness was correctly prescribed, their model reproduced the observed ice thickness and temperature profiles in snow and ice with differences not exceeding 3 °C. They underlined the sensitivity of the ice thickness to the ocean heat flux and to the snow cover in winter. Using the LIM1D model, Lecomte et al. (2011) tested a new snow

thermodynamic scheme at point Barrow (Alaska) and at Ice Station POLarstern in the western Weddell Sea. They emphasized the need for several snow layers (between three and six) for a precise estimation of the temperature inside the snow. Duarte et al. (2017) simulated the spring ice mass balance data from the N-ICE2015 expedition with the Los Alamos sea ice model (CICE) and reproduced the ice temperature with a root-mean-square difference (RMSD) of 0.47 °C. Dupont et al. (2015) compared sea ice representation through different numerical approaches and concluded that the Bitz and Lipscomb (1999) finite difference approach, the sigma-coordinate model of Huwald et al. (2005), and its variant based on finite elements all converge to the same solution.

In this study, we combine high-resolution winter Arctic observations with the snow and ice model LIM1D (Vancoppenolle et al., 2008). The observations were collected during the Norwegian young sea ICE expedition (N-ICE2015), which provided an observing platform for atmosphere, snow, sea ice, and ocean from January to end of June 2015, north of Svalbard (Granskog et al., 2016). The winter observations from Sea Ice Mass Balance instruments (SIMBA) showed abundant snowfalls and intense basal sea ice melt. They also provided the first documentation of significant flooding and snow ice formation in the Arctic ice pack (Provost et al., 2017; Figure 1).

The main aim of this study is to revisit these high-resolution winter Artic data series with a modeling point of view, to improve our understanding of the physical processes within sea ice and snow. We simulated snow and sea ice temperature profiles over two SIMBA drifts. A few sensitivity studies guided our choice of atmospheric and oceanic forcing, snow conductivity parameterization, and initial ice salinity. The joint use of the simulated and observed temperature profiles allowed adjustments of the snow density profiles. Once a good agreement between observed and simulated temperature profiles was reached, we analyzed salinity and brine volume fraction (physical properties that cannot be measured continuously). In particular, flooding events were simulated and salinity and brine fraction were used to investigate the process of snow ice formation.

The paper is organized as follows. Section 2 describes the model, the observations, and the forcing terms. A reference run and sensitivity studies are presented in section 3. In section 4, snow density profiles are adjusted combining data and simulations. The processes of flooding and subsequent snow ice formation are analyzed in section 5. Finally, section 6 summarizes the results and provides perspectives.

## 2. Model and Observations

### 2.1. The LIM1D Model

The LIM1D model described in Vancoppenolle et al. (2008, 2010); Vancoppenolle and Tedesco (2017) is based on the enthalpy conserving scheme proposed by Bitz and Lipscomb (1999). We summarize its main characteristics, emphasizing aspects that are pertinent for this study.

In its simplest configuration, the model computes at each time step $t$ and depth $z$ the following fundamental quantities:

snow temperature $T_s(z,t)$,

ice temperature $T(z,t)$ and bulk salinity $S(z,t)$,

sea ice thickness $h(t)$.

The model solves the heat equation in snow and sea ice and a supplementary advective-diffusive equation for the salt in sea ice (Vancoppenolle et al., 2010). The heat equation reads:

$$\rho_i c \frac{\partial T}{\partial t} = \frac{\partial}{\partial z}\left(k \frac{\partial T}{\partial z}\right) + Q_{sw} \tag{1}$$

where $c = 2{,}060$ J/kg/K is the ice specific heat, $\rho_i$ is the ice density ($\rho_i = 917$ kg/m$^3$), $k$ is the ice conductivity (W/m/K), and $Q_{sw}$ is the absorption of solar radiation.

The equation for salinity conservation in sea ice is

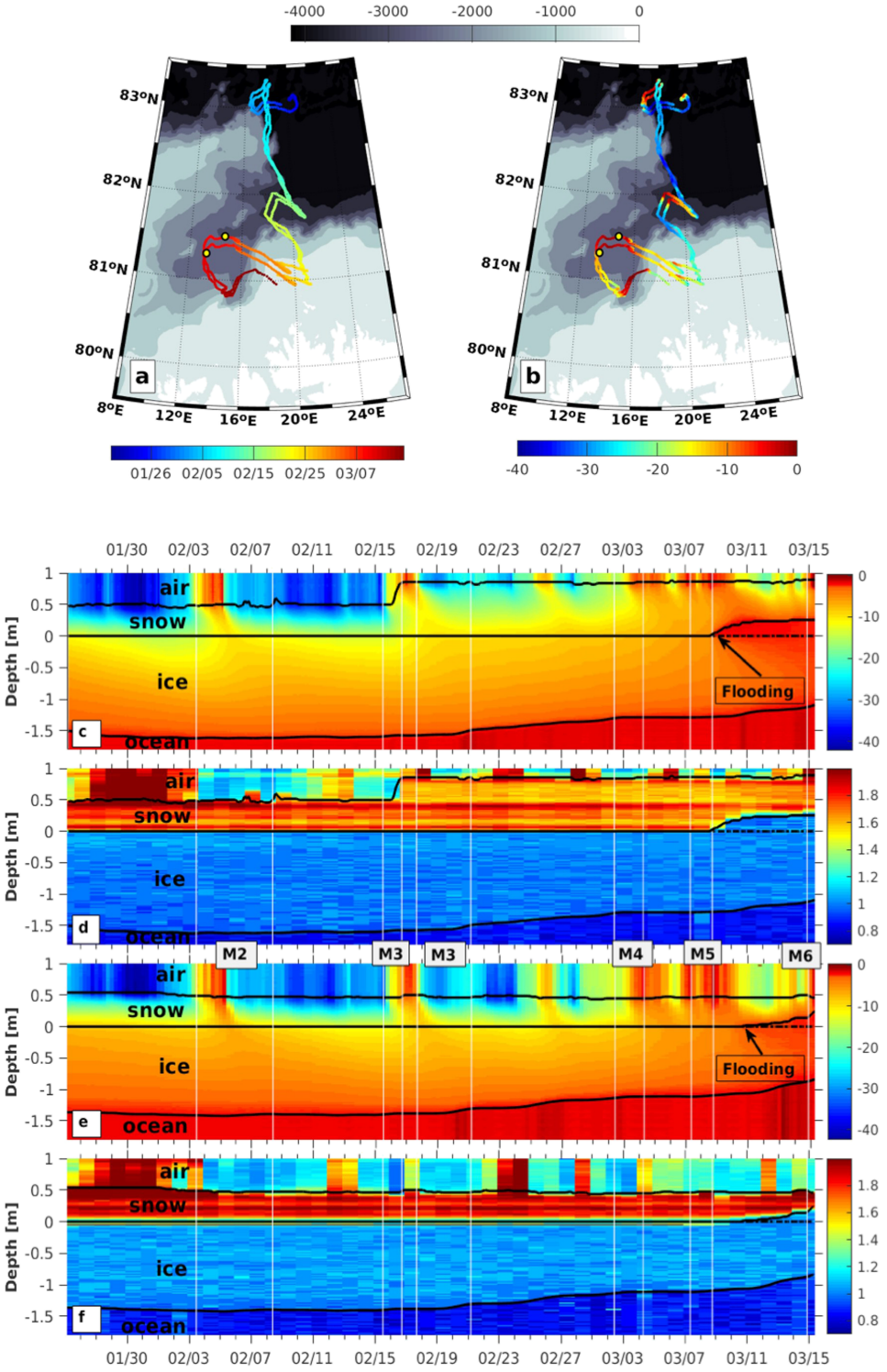


**Figure 1.** (a) Time and (b) air temperature along the SIMBA_a and SIMBA_h drift trajectories (°C). The background is bathymetry (m). Yellow circles indicate the onset of the flooding events. (c) Temperature (°C) as a function of time for SIMBA_h. (d) Thermal diffusivity proxy* (no units) as a function of time for SIMBA_h. (e) Same as (c) for SIMBA_a. (f) Same as (d) for SIMBA_a. Vertical resolution is 2 cm. Black lines correspond to the air/snow interface, the lower limit of the snow layer and ice/ocean interface. Temperature color scale is nonlinear in order to highlight temperature changes in the ocean. Storms are labeled M2, M3, … , M6 as described in Cohen et al. (2017). * The heating mode produces a heat pulse and the temperature response to the heat pulse depends on the medium and provides the diffusivity proxy (Jackson et al., 2013).

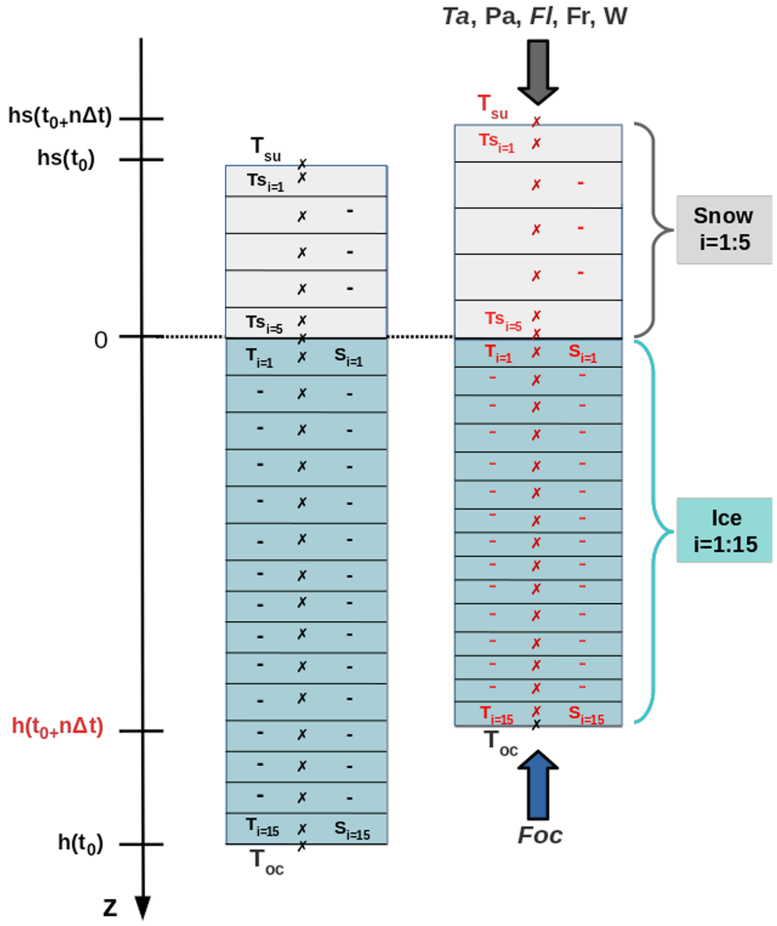


**Figure 2.** Schematics of LIM1D model. Five snow layers of equal thickness (gray) and 15 sea ice layers of equal thickness (blue) evolve over time. Initial condition ($t_0$) and prescribed values are in black, and calculated values at each time step (t) are in red. $h_s$: snow thickness, $h_i$: ice thickness, $T_A$: air temperature, $P_A$: sea level pressure, $F_L$: long-wave flux, $F_R$: short-wave flux, $W$: wind, $T_S$: snow temperature $T_i$: ice temperature, $T_{OC}$: ocean temperature, $F_{OC}$: ocean flux, $S_i$: ice salinity. The time step of the model is 1 hr.

$$\frac{\partial S}{\partial t} = -\nu_z \frac{\partial S}{\partial z} + \frac{\partial}{\partial z}\left[D_\sigma \frac{\partial S}{\partial Z}\right] \tag{2}$$

with $\nu_z$ being the vertical velocity of the fluid within the brine network (m/s) and $D_\sigma$ the salt diffusivity in water ($m^2/s$).

The system is divided into a fixed number of layers in the ice and snow, as indicated in Figure 2. At each time step, enthalpy and salinity are redistributed to follow the thickness changes in such a way that the enthalpy and the salt content are conserved. Other physical quantities (such as the brine volume fraction $e(z,t)$ in the sea ice and the brine salinity $\sigma(z,t)$) are derived from the fundamental ones. The initial values $h(t_0)$, $T(z, t_0)$, $S(z, t_0)$, and $T_s(z, t_0)$ are prescribed. Various quantities are necessary to force the model.

Atmospheric heat fluxes are required at each time step of the integration. Incoming short-wave radiation $F_r$ and incoming long-wave radiation $F_L$ are introduced in the model through the following boundary condition, applied at the upper boundary of the snow, $z = h_S(t)$:

$$-k_s \frac{\partial T}{\partial z} = (1-\alpha)F_r - I_0 + F_L + \epsilon_L \sigma_S T_{surf}^4 + F_S + F_{La} \tag{3}$$

where $\alpha$ is the surface albedo ($\alpha = 0{,}85$), $I_0$ is the incoming short-wave radiation that penetrates through the

snow ($I_0 = 0.22(1-\alpha)F_R$), $\varepsilon_L$ is the emissivity ($\varepsilon_L = 0.95$), $\sigma_S$ is the Stefan constant ($\sigma_S = 5.67.\ 10^{-8}$ W/m$^2$/K$^4$), $k_S$ is the snow conductivity (W/m/K), and $F_{\mathrm{La}}$ is the latent heat flux (W/m$^2$).

The surface temperature of the snow $T_{\mathrm{surf}}(t)$ (equation (3)) is computed by the model. It differs from the air temperature $T_a(t)$, which is prescribed and permits to compute the sensible heat flux $F_S$ (W/m$^2$):

$$F_s(t) = C_p \rho_a\, u_a C_H (T_{\mathrm{surf}}(t) - T_a(t)) \tag{4}$$

where $u_a$ is the wind velocity (m/s), $\rho_a$ the air density ($\rho_a = 1.275$ kg/m$^3$), $C_p$ the air specific heat ($C_p = 1{,}005$ J/kg/K), and $C_H$ the bulk transfer coefficient for sensible heat at neutral stability ($C_H = 1.75 \times 10^{-3}$). The coefficient $C_H$ depends on the surface roughness parameter and on the wind speed (Andreas, 1987). The use of this constant value has been a common strategy since (Maykut, 1978).

The latent heat flux $F_{\mathrm{La}}$ (equation (3)) is proportional to the difference $q_s - q_a$, where $q_s$ is the surface humidity and $q_a$ the prescribed air humidity (kg/kg). $F_{\mathrm{La}}$ is small in comparison with the other fluxes.

At each time step of the integration, the evolution of the sea ice thickness is computed by satisfying the boundary condition at the lower boundary of the sea ice $z = h_i(t)$:

$$-\mathrm{k}\frac{\partial T}{\partial z}\bigg|_i - \rho_i L \frac{\mathrm{dh}}{\mathrm{dt}} = F_{\mathrm{OC}} \tag{5}$$

where $F_{\mathrm{OC}}$ is the ocean heat flux and $L$ the latent heat of fusion of ice ($L = 333.5 \times 10^3$ J/kg). The temperature at the base of the sea ice $T(h(t), t)$ is also prescribed. This is equivalent to prescribing the ocean salinity $S_{\mathrm{OC}}(t)$ via the approximate liquidus relation $T(h(t), t) = -\mu \mathrm{S}_{\mathrm{OC}}(t)$, where $\mu$ is a constant ($\mu = 0.054$ ° C/‰).

We decided to prescribe the upper limit of the snow (this is here equivalent to prescribing the local snowfall) instead of the ERA-I precipitation; the observed snow thickness depends upon the location of the SIMBA on the floe (local accumulation, wind, and snow deposition; Provost et al., 2017). We also prescribed the lower limit of the snow. Using the Archimedes' principle, the 1-D model computes the position of the local waterline (or equivalently the height between the snow base and the waterline: the freeboard). In the experiments, the simulated waterline was above the snow ice interface, which induced an intrusion of seawater into the snow layer. The local position of the waterline depends on the global characteristics of the floe (the size of the floe, the snow cover and ice thickness, and the ice rheology). Prescribing the lower limit of the snow (at $z = 0$) prevents the seawater intrusion; before the flooding, the lower limit of snow was the snow/ice interface and after, the snow/slush interface.

The density of the snow $\rho_s$ can be adjusted. The snow conductivity is given by Abel's relation $k_s = 2.846 \times 10^{-6} \rho_s^2$.

In the ice, the salinity of brine pockets $\sigma(z,t)$ is computed from the temperature of sea ice using the liquidus relation $T(z,t) = -\mu\sigma(z,t)$. The brine fraction $e(z,t)$ represents the amount of liquid water in the ice and depends on the bulk salinity $S(z, t)$ and the local ice temperature $T(z, t)$:

$$e(z,t) = \frac{S(\mathrm{z},\mathrm{t})}{\sigma(\mathrm{z},\mathrm{t})} = -\mu \frac{S(\mathrm{z},\mathrm{t})}{T(\mathrm{z},\mathrm{t})} \tag{6}$$

The ice conductivity $k(z,t)$ and specific heat $cz,t)$ have a complex expression deduced from empirical measurements (Pringle et al., 2007):

$$k(z,t) = 2.11 + 0.09 \frac{S(\mathrm{z},\mathrm{t})}{T(\mathrm{z},\mathrm{t})} - 0.011\ \mathrm{T}(z,t) \tag{7}$$

and

$$c(\mathrm{z},\mathrm{t}) = 2062 + L\mu \frac{\mathrm{S}(\mathrm{z},\mathrm{t})}{T(\mathrm{z},\mathrm{t})^2} \tag{8}$$

where the temperature $T(z, t)$ is in degrees Celsius (°C).

These relations control the impact of salinity on the evolution of the temperature profile in the ice.

The continuity of the heat fluxes between ice and snow is imposed:

$$-k_s \frac{\partial T}{\partial z}\bigg|_s = -k \frac{\partial T}{\partial z}\bigg|_i \tag{9}$$

The heat equation (1) provides a first estimation of the temperature profile at $t_{i+1} = t_i + \delta t$ from their values at $t_i$ ($\delta t = 1h$)using the boundary condition (equation (3)) and the prescribed value $T(h(t), t) = T_{oc}$. Because the term $\epsilon_L \sigma_S T_{surf}^4$ is nonlinear, an iterative implicit method is used. Then the equation for salinity is solved (Vancoppenolle et al., 2010). The ice thickness is computed from equation (5). The temperature and salinity profiles are then modified in such a way that the enthalpy of the system composed of new snow, old snow, and sea ice is conserved. All numerical experiments shown here were performed with 15 layers of sea ice and 5 layers of snow (Figure 2).

### 2.2. Observations

The Research Vessel Lance (RV Lance) drifted with the Arctic ice pack from January to end of June 2015, north of Svalbard (Granskog et al., 2016). Throughout winter 2015, the Arctic vortex was strong with large amount of northward air volume transport over the Greenland Sea. Six synoptic events (storms) characterized by strong winds occurred and brought warm air from the south and heavy precipitation (Graham et al., 2016; Hudson & Cohen, 2016). Precipitation rates based on ERA-Interim reanalysis (Dee et al., 2011) showed that winter 2015 faced exceptionally abundant snowfalls; the one of February 2015 was the second largest in the ERA-Interim reanalysis record (1979–2015) for the N-ICE2015 region (Merkouriadi et al., 2017).

Seven SIMBAs recorded repeated profiles of temperature and thermal diffusivity proxy (Provost et al., 2017). We focused on the two longest SIMBA time series called SIMBA_a and SIMBA_h (Figure 1). The SIMBA data showed limited sea ice growth until mid-February and intense basal sea ice melt when the ice floe drifted over the warm Atlantic waters on the continental slope north of Svalbard. The ocean-to-ice fluxes peaked at 300 W/m$^2$ and induced a 0.50 m loss of ice in one month (Figures 1c–1f). The SIMBAs also provided the first documentation of significant flooding and snow ice formation in the Arctic ice pack. Flooding was a consequence of negative freeboard conditions due to a heavy snow load relative to the ice thickness and a storm-induced breakup of the floes. From isotope analysis of 29 ice cores collected during the N-ICE 2015 expedition, Granskog et al. (2017) estimated that snow ice contributed to 7.5–9.7% of the sea ice mass balance on average.

### 2.3. Model Forcing

#### 2.3.1. Atmospheric Forcing

The long-wave flux $F_L$, the short-wave flux $F_r$, and the air temperature $T_a$ are available from the global reanalysis ERA-Interim (ERA-I), with a 6 hr time resolution (Figure 3, red curves in panels a–c; Dee et al., 2011). Because of the polar night, $F_S$ was null until March; then it slowly increased with a strong diurnal daily cycle, without exceeding 45 W/m$^2$ (Figure 3b).

The long-wave fluxes $F_L$ and $F_r$ are also available from direct measurements made on the RV-Lance with a 30 min time resolution (Hudson & Cohen, 2016; Figure 3a, black curve). Measurements from the ship could only be used before 20 February, when the ship was forced to relocate northward after a massive floe breakup. During the drift, $F_L$ varied between 120 and 300 W/m$^2$ and exhibited variations largely correlated with the air temperature (Figures 3a and 3c). Air temperature is also available with a 1 hr resolution from the IAOOS7 (Ice Atmosphere Ocean Observing System) buoy on which SIMBA_h was installed (Koenig et al., 2016; Figure 3c, blue curve). The air temperature ranged from −42 to 0 °C and exhibited sudden peaks associated with the storms, in addition to a gradual warming trend throughout the observation period. ERA-I air temperature is larger than the observed one during cold winter conditions (by 8 °C) and smaller during warm periods (by −5 °C; Cohen et al., 2017).

The wind speed at 10 m is available from ERA-I with a 6 hr resolution. It varied between 2 and 21 m/s (Figure 3d), and the large wind speeds correspond to the storm events described in Cohen et al. (2017). The largest values were correlated to the increase of temperature and long-wave flux (Figures 3a, 3b, and 3d).

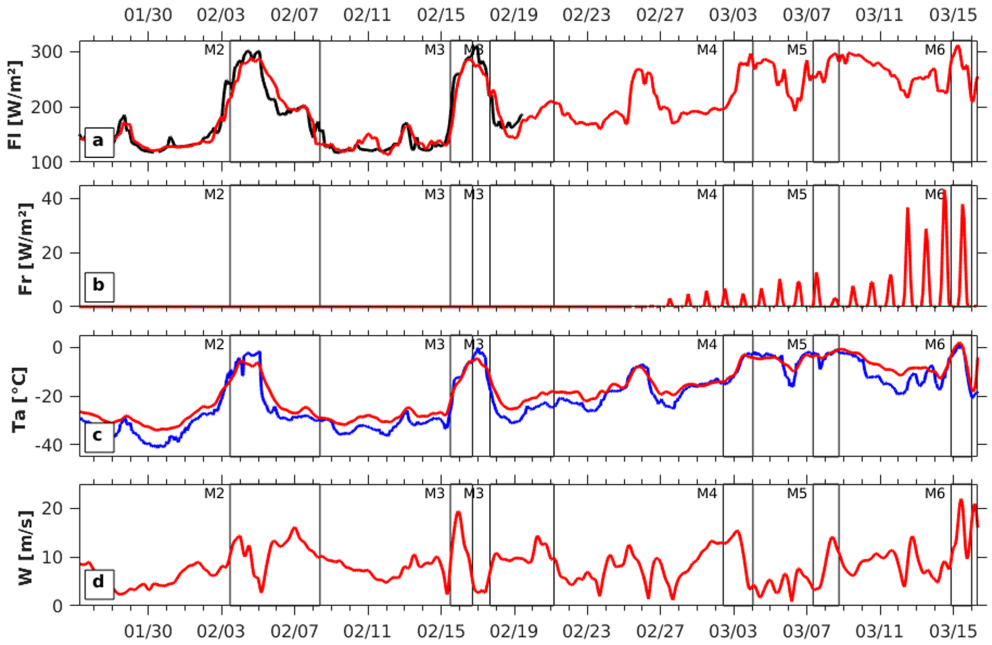


**Figure 3.** Time series of the atmospheric forcings: (a) long-wave flux from ERA_I (red) and RV_LANCE (black), (b) short-wave flux from ERA_I, and (c) air temperature (blue: from the IAOOS central unit; red: from ERA_I). (d) Wind speed from ERA_I. Storms are labeled M2, … , M6 as described in Cohen et al. (2017).

All the data series (ERA-I, RV-Lance) have been interpolated to fit the 1 hr time step of the model.

#### 2.3.2. Forcing Deduced From SIMBA Snow and Ice Observations

SIMBA_a and SIMBA_h recorded different values of snow and ice thickness (Figure 4a). At the SIMBA_h site, the snow thickness remained nearly constant (around 55 cm) then increased by about 40 cm at the beginning of storm M3 and did not evolve much until 8 March (blue curve, Figure 4a). At SIMBA_a site, the snow thickness remained constant the first 6 days and lost 10 cm at the beginning of the M2 storm. Then, it remained mostly constant (around 45 cm) until 9 March, when a flooding began (red curve, Figure 4a).

The lower limit of the snow (referenced to its initial value $z = 0$) remained unchanged until the seawater invaded the snow (storm M5) and reached a maximum value of 34 cm at SIMBA_h site (24 cm at SIMBA_a). As previously indicated, the lower limit of snow was used to trigger and control the flooding event.

The ocean temperature $T$oc ranged between −2 and −0.7 °C for SIMBA_a and −1.9 and −1.2 °C for SIMBA_h (Figure 4c). A systematic difference of 0.1 °C is visible in Figure 4. A comparison with the five other SIMBAs in the vicinity (Provost et al., 2017; shorter time series, not shown) outlined a cold bias in SIMBA_a temperature, which has been corrected. Before 19 February, the ocean temperature was more or less constant and close to the ocean freezing temperature, for both buoys. After 19 February, the two buoys drifted over warmer water above the continental slope north of Svalbard. The ocean heat flux $F_{OC}$ computed from the melting rate of sea ice and the sensible heat flux (Provost et al., 2017) for SIMBA_a and SIMBA_h varied between −100 and 300 W/m$^2$ and followed the ocean temperature variations (Figure 4d).

## 3. Reference Run and Sensitivity Studies for SIMBA_h

### 3.1. Reference Run

The reference run was initialized with snow thickness, sea ice thickness, and temperature profile observed on 26 January (Figure 5a, left). The initial bulk salinity profile was taken from an ice core collected close to the buoy SIMBA_h (83.5°N, 18.9°E) on 26 January (Granskog et al., 2017; Figure 5c, left). We chose the classic values of 2062 J/kg/K for the snow specific heat and 917 kg/m$^3$ for the pure ice density. According to the

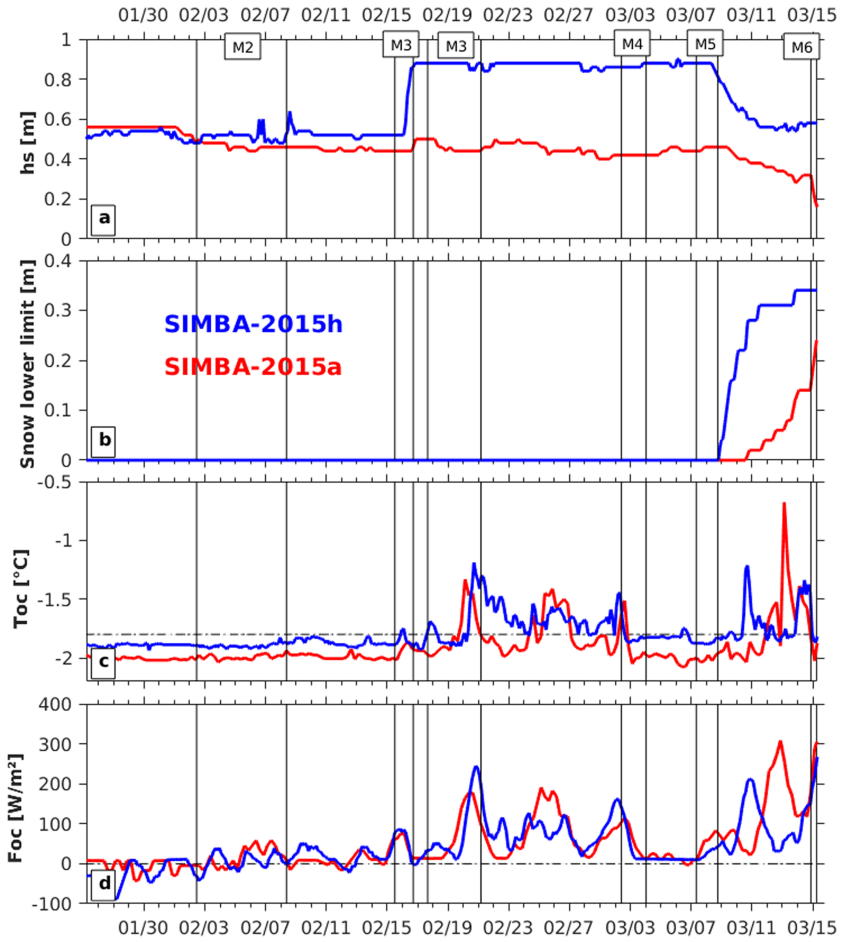


**Figure 4.** Time series derived from SIMBA observations (Provost et al., 2017; blue curve for SIMBA_h and red curve for SIMBA_a): (a) snow thickness, (b) lower limit of the snow layer on the SIMBA chain, (c) ocean temperature, and (d) ocean heat flux. Storms are labeled M2, ... , M6 as described in Cohen et al. (2017).

observations, the snow density was 390 kg/m$^3$ (Merkouriadi et al., 2017). The associated conductivity was 0.43 W/m/K. The reference run was forced with ERA-I long-wave and short-wave flux and the IAOOS7 air temperature (Table 1).

Until the flooding event, the simulated ice thickness never differed from the observations by more than 2 cm (not shown), the observed thickness uncertainty. This result shows the consistency of the ocean heat fluxes computed by Provost et al. (2017).

The simulated temperature profiles were close to the observations (Figures 5a and 5b) with a RMSD between the observed and simulated temperature of 1.06 °C in the snow and 0.19 °C in the ice (Table 2). The storms induced an increase of the snow surface temperature, which then diffused through snow and ice. The lower boundary of the snow was prescribed to trigger the flooding event of 8 March. The snow located under this limit was filled with seawater at the freezing temperature, leading to a rapid increase of the temperature at the snow/ice interface (from −5.9 to −1.9 °C in less than 5 hr). The flooding impinged on the surrounding ice down to 0.60 m depth with an ice temperature increase of about 2 °C.

Temperature differences with the observations never exceeded ±3 °C in the snow and were maximum close to the snow/air interface (Figure 5b), suggesting atmospheric fluxes as possible source of error. The temperature difference between simulation and observation in the sea ice never exceeded ±1.2 °C (0 to 0.5 °C during most of the run, Figure 5b). The temperature of the slush layer associated with the flooding was also well represented. The temperature difference between model and observation was lower than 0.4 °C in the slush layer and surrounding ice.

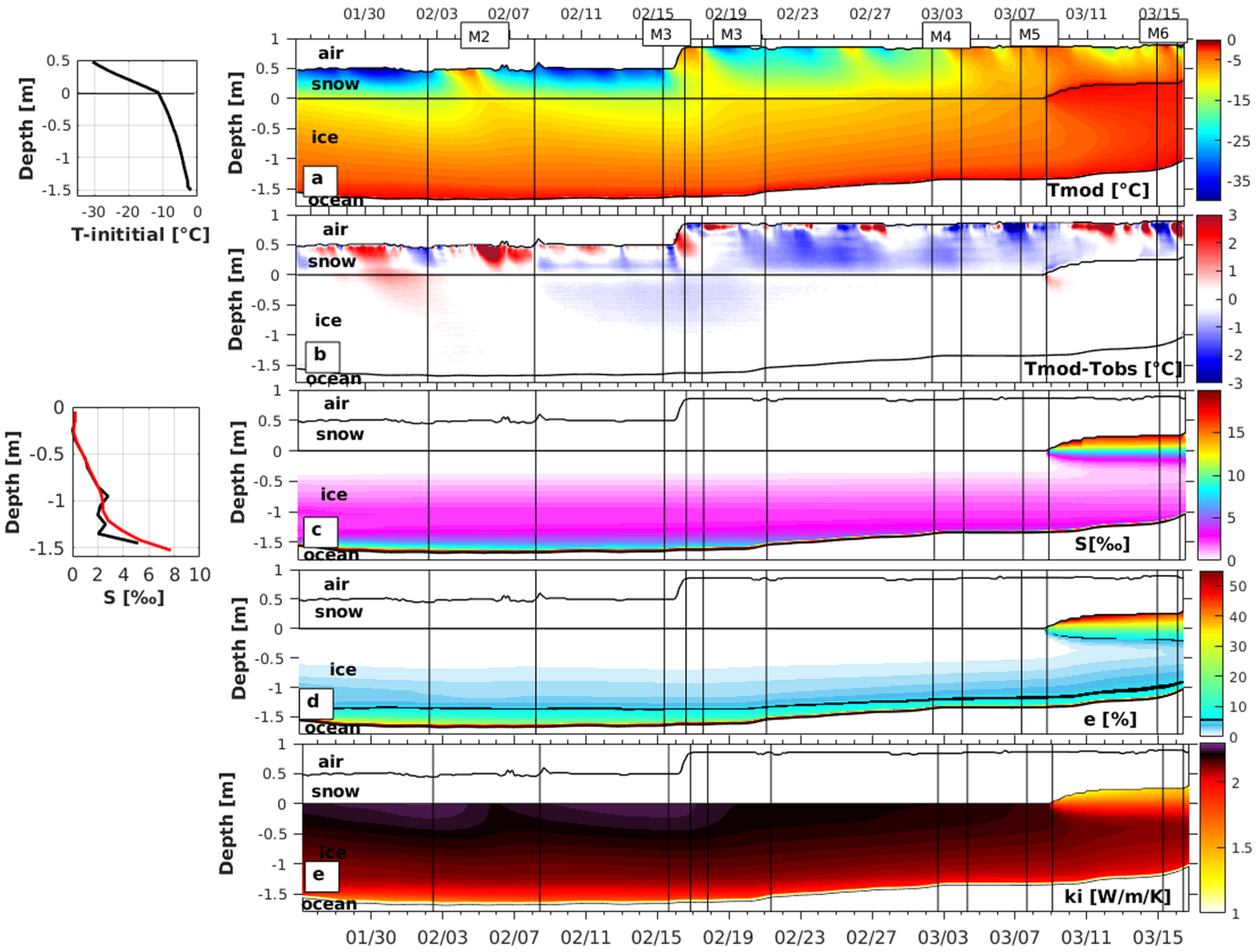


**Figure 5.** Reference run for SIMBA_h. (a) Left: initial observed temperature profile in snow and ice. Right: simulated temperature as a function of time in snow and ice. (b) Temperature differences between simulation and observations. Model outputs are interpolated to the vertical resolution of the data (2 cm). (c) Left: initial observed ice salinity profile (black) from Granskog et al. (2017) and simulated salinity profile on 26 January (red). Right: simulated ice salinity as a function of time. (d) Simulated ice brine fraction as a function of time. The black isoline corresponds to the 5% brine fraction. (e) Time series of the simulated ice conductivity. On all the panels, black lines correspond to the air/snow interface, the lower limit of the snow layer and ice/ocean interface. Storms are labeled M2, M3, ... , M6 as described in Cohen et al. (2017).

The simulated salinity profiles rapidly became smoother than the observed initial profile (Figure 5c, left). The bulk salinity remained close to 0‰ at the snow/ice interface and increased with depth to 2.5‰ at 1.0 m depth (Figure 5c). In the lowermost 5–10 cm, the bulk salinity increased to reach the prescribed value at the ice/ocean interface. When flooding began, salinity of the immersed snow layer drastically increased: the salinity of the slush layer reached 19‰ (Figure 5c).

**Table 1**
*Forcing and Initial Conditions for the Reference Run (First Column) and the Different Simulations for the Sensitivity Studies (the Modified Characteristics With Respect to the Reference Run Is Indicated)*

| | Reference run | Run A | Run B | Run C | Run D | Run E |
|---|---|---|---|---|---|---|
| Oceanic flux | Provost et al. (2017) | Smoothed noisy constant | | | | |
| Long-wave flux | ERA-I | | R/V Lance | | | |
| Air temperature | IAOOS buoy | | | ERA-I | | |
| Initial ice salinity profile | Granskog et al. (2017) | | | | 5‰ | |
| Snow conductivity | Abel's | | | | | Sturm et al. (1997) |

**Table 2**
*Root-Mean-Square Difference Between the Observed and Simulated Temperature in Snow and Ice for the Reference Run and the Runs Corresponding to the Sensitivity Studies (°C)*

| RMSD (°C) SIMBA_2015h | Reference run | Run B | Run C | Run D | Run E |
|---|---|---|---|---|---|
| **Snow layer** | | | | | |
| **Entire run** | 1.06 | / | 2.00 | 1.17 | 1.58 |
| **Part 1 (until 19 February)** | 1.01 | 0.92 | 1.61 | 1.17 | 1.36 |
| **Ice layer** | | | | | |
| **Entire run** | 0.19 | / | 0.26 | 0.35 | 0.84 |
| **Part 1 (until 19 February)** | 0.23 | 0.24 | 0.33 | 0.31 | 0.77 |

*Note*. The statistical significance of the difference between each sensitivity study and the reference run was assessed using a Fisher test on the RMSD. They all passed the test at the 95% CL.

The brine fraction is the relative volume of salty water in the ice. For a brine fraction larger than 5%, sea ice is considered as permeable and brine pockets are interconnected (Golden et al., 1998). With a brine fraction between 50% and 60%, ice becomes mobile, forming a cohesive slush; with a brine fraction over 60%, ice has no more cohesion and becomes a loose slush (Jutras et al., 2016). Most of the simulated ice layer had a brine fraction smaller than 5% (Figure 5d). Brine fraction increased near the ice base (over 10 cm) and reached 97% at the ice/ocean interface (for salinity = 34‰, $T = -1.84$ °C). The cohesive slush was approximatively 1 cm thick, and the last 3 cm above the open ocean were made of loose slush. The brine fraction at 0.5 m depth increased from 0% to 5% at the end of the simulation (Figure 5d). The brine fraction in the ice, near the snow/ice interface, was close to zero before 8 March and reached a maximum of 20% after the infiltration of salty seawater in the snow layer. The flooding and the resulting snow ice formation are studied in section 5.

The ice thermal conductivity is controlled by salinity and temperature (equation (7)). When the temperature at the snow/ice interface increased, the ice conductivity decreased (Figure 5e). On 4 February, the air temperature suddenly rose up to −2 °C, leading to a decrease of the ice conductivity, from 2.4 to 2.1 W/m/K at the snow-ice interface (Figure 5e). The salinity at the snow ice interface ($z = 0$) drastically increased when flooding occurred, leading to a decrease of the conductivity from 2.1 to 1.6 W/m/K.

### 3.2. Sensitivity Studies

We performed simulations to evaluate how changes in the external forcing, initial salinity profile, and snow conductivity may affect the simulated snow and sea ice temperature profiles. Table 1 summarizes the different simulations, and Table 2 provides the RMSD between the observed and simulated temperatures in snow and ice.

#### 3.2.1. Oceanic Flux

Usually, when the ocean heat flux is not available, a constant value is used to force sea ice models. Here, the ocean heat flux computed by Provost et al. (2017) is available with a 3 hr time resolution. This provided the opportunity to evaluate the impact of the time resolution of the oceanic heat flux on the simulation.

We used three different ocean heat fluxes: constant, smoothed, and noise-added fluxes (Figure 6a). The smoothing was obtained with a 10-day running mean. The added white noise had an amplitude of 112 W/m$^2$, which is twice the oceanic flux estimate uncertainty (Provost et al., 2017). The three heat fluxes had the same mean value as the reference ocean flux (48 W/m$^2$). The RMSD with the reference oceanic flux is 32 W/m$^2$ for the smoothed flux and 56 W/m$^2$ for the constant and the noise added fluxes.

The final ice thickness was the same in all simulations as all ocean fluxes had the same mean over the time period (Figure 6b). The constant flux led to a continuous basal melt, and the ice thickness difference with the reference run reached 30 cm on 19 February (blue curve in Figure 6b). The largest impact on the ice thickness of the smoothed flux occurred during the intense basal melt (6 cm on 15 March), while the impact of the noise added flux never exceeded 2 cm (the vertical precision of the observed ice thickness; Figure 6b). The impact of the ocean heat flux time resolution on ice temperature can only be estimated for the smoothed and noise-added fluxes and never exceeded 0.2 °C (not shown).

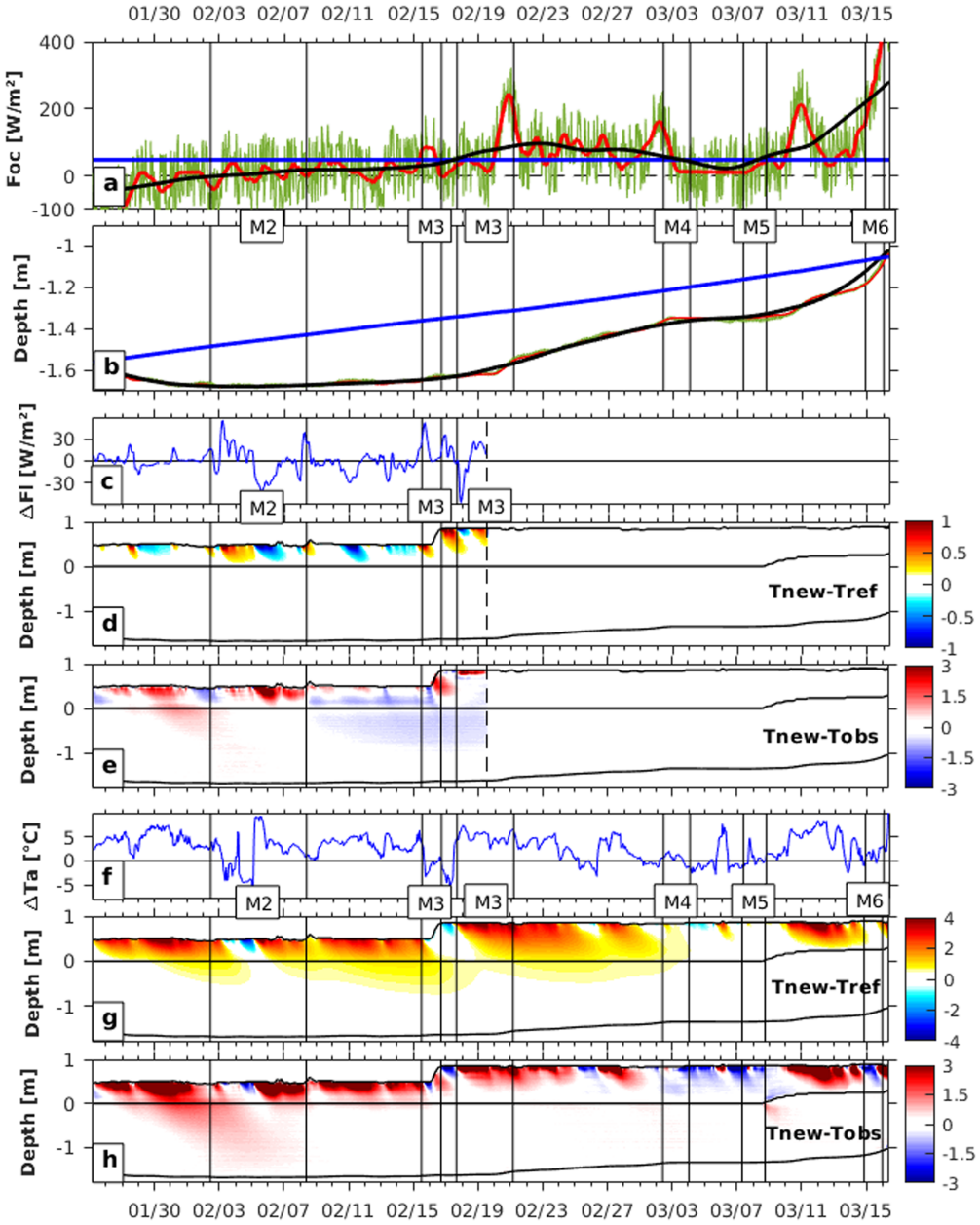


**Figure 6.** (a) Reference ocean heat flux (red), smoothed ocean heat flux (black), noise-added ocean heat flux (green), and constant ocean heat flux (blue). (b) Simulated ice thickness obtained with the reference (red), smoothed (black), noise added (green), and constant (blue) ocean heat flux (green). (c) Difference between RV Lance (available until 02/20) and ERA-I long-wave fluxes. (d) Temperature difference (°C) between the simulation forced with the long-wave flux from RV Lance and the reference simulation (ERA-I). (e) Temperature difference (°C) between simulation (using RV-LANCE long-wave flux) and observations. (f) Difference between ERA-I and IAOOS air temperature. (g) Temperature difference (°C) between the simulation forced with ERA_I air temperature and the reference simulation (IAOOS). (h) Temperature difference (°C) between simulation (using ERA_I air temperature) and observations. Storms are labeled M2, M3, … , M6 as described in Cohen et al. (2017).

In this particular winter case (slow ice growth followed by an intense basal ice melt), the simulated ice thickness and temperature were not very sensitive to the short timescale variations of the ocean heat flux. However, smoothing over 10 days prevented a precise representation of its variations (mostly during intense basal melt).

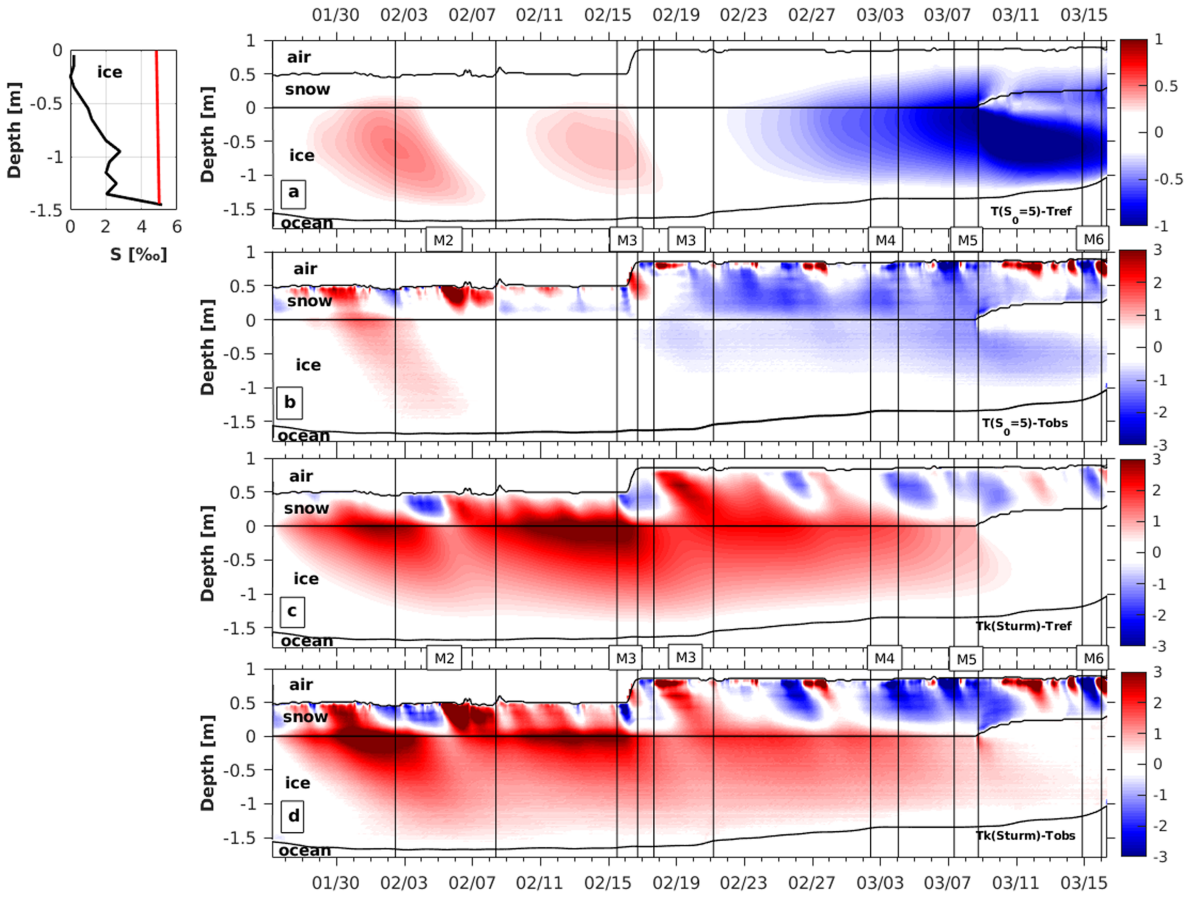


**Figure 7.** (a) Left: observed initial ice salinity used for the reference run (black; Granskog et al., 2017) and uniform initial salinity of 5‰. Right: temperature difference between the simulation with a uniform initial salinity of 5‰ and the reference simulation. (b) Temperature difference (°C) between simulation (initial salinity of 5‰) and observations. (c) Temperature difference between the simulation with a snow conductivity deduced from Sturm et al. (1997) and the reference one (°C). (d) Temperature difference between simulation (using Sturm et al., 1997, conductivity) and observations. Storms are labeled M2, M3, ... , M6 as described in Cohen et al. (2017).

### 3.2.2. ERA-I and RV-Lance Incoming Long-Wave Radiation

We compared the reference simulation (obtained using the ERA-I long-wave heat flux) to a simulation forced by the long-wave heat flux measured on the RV-Lance. The comparison only covered the first 25 days of the simulation since the RV-Lance had to relocated after 19 February. ERA-I and RV-Lance long-wave flux both have a mean value of 170 W/m$^2$ and a standard deviation of 50 W/m$^2$. The RMSD between the two series is 12 W/m$^2$.

Temperature differences between the two simulations varied between ±1 °C at the snow/air interface and, as expected, were strongly correlated with the flux differences (Figures 6c and 6d). Using the observed fluxes from RV-Lance slightly improved the run (Figure 6e): The RMSD between the observed and simulated snow temperature was smaller (0.92 °C) than in the reference run (1.01 °C) (Table 2). Even if using the RV-Lance long-wave flux improved the simulation, the impact remained small in the snow layer and negligible in the ice: The thick isolating snow cover (~50 cm) prevented the emergence of temperature variations in the ice. This comparison suggests that the use of ERA-I long-wave flux is reasonable in this case (thick snow cover).

### 3.2.3. ERA-I and IAOOS Air Temperature

We performed a simulation using ERA-I air temperature at 2 m. ERA-I air temperature was too large during cold period (up to 10 °C) and too small during warm period (up to 5 °C; Figure 6f), leading to a RMSD of 3.3 °C with the observed air temperature (Graham et al., 2016). The RMSD between the observed and simulated temperature increased to 2.0 °C for the snow and 0.26 °C for the ice (Figure 6h and Table 2). As expected, the temperature differences between the reference run and the ERA-I air temperature run were maximum at the

air/snow interface (4 °C) and decreased with depth: They did not exceed 1 °C at the snow/ice interface and 0.5 °C, approximately 50 cm below (Figure 6g).

The impact of the ERA-I air temperature was significant in the ice, even with 50 cm snow cover. It could be more important with less snow. The results show the importance of using accurate observation of the air temperature to force the model. Degrading the time resolution (12 hr moving average) of the air temperature did not modify significantly the simulation (not shown).

#### 3.2.4. Uniform Versus Observed Initial Salinity Profile

We performed a simulation using a uniform initial ice salinity of 5‰ (Figure 7a, left). This is the common value of salinity used in sea ice models when the observed one is not available (Schmidt et al., 2004; Zhang & Rothrock, 2001). The simulation was altered, with a RMSD between the observed and simulated temperature of 1.17 °C for the snow and 0.35 °C for the ice (Figure 7b and Table 2, Run D). A larger salinity is expected to have a direct impact on the temperature, by reducing the sea ice thermal conductivity (equation (7)).

During the first period (before 19 February), the new simulation was warmer than the reference (up to 0.5 °C), as the smaller conductivity inhibited the penetration of the cold air temperature (Figure 7a). The effect of the uniform salinity on the ice temperature was reduced during storms, since the air temperature increased (M2 and M3, Figure 7a).

During the second period, the thick snow cover (≈80 cm) better insulated the sea ice from the air temperature and the uniform salinity profile had an opposite effect on the ice temperature (and snow). The temperature differences between simulation and observation were maximum when flooding occurred; the simulated ice temperature was colder than observations, by about 1 °C down to 80 cm.

#### 3.2.5. Snow Conductivity

We used the parameterization of snow conductivity proposed by Sturm et al. (1997):

$$k\mathrm{S2} = 0.138 - 1.01\,\rho S + 3.223\,\rho S2 \text{ valid in the range } 156 < \rho S < 600\ \mathrm{kg/m^3}$$

which leads to significantly different snow conductivity: For a snow density of 390 kg/m$^3$, conductivity reduces from 0.43 W/m/k if computed with Abel's formula (used in the reference run) to 0.23 W/m/k.

During cold periods, as expected, the snow with the small conductivity was warmer than in the reference run: Temperature differences with the reference run increased with depth and reached a maximum at the snow-ice interface (around 3 °C; Figure 7c). The impact of the small snow conductivity was still observed 1 m below the snow-ice interface (about 1 °C). During warm episodes (e.g., 3, 16, and 26 February and 7 and 15 March), the snow (with the small conductivity) was colder than in the reference run by almost 2 °C, as the small conductivity inhibited heat penetration (Figure 7c). Just before flooding, the temperature difference at the snow ice interface was 0.5 °C. The heat flux during flooding was due to the intrusion of seawater, limiting the impact of the change in snow conductivity.

The use of Sturm et al. (1997) parameterization of snow conductivity deteriorated the simulation in snow and ice (Figure 7d and Table 2, Run E): The RMSD between the observed and simulated temperature was 1.58 °C for the snow and 0.84 °C for the ice. Using Sturm et al. (1997) equation without deteriorating the simulation would have implied to assume a snow density of 500 kg/m$^3$, which was not consistent with the measurements made during the N-ICE2015 campaign (Merkouriadi et al., 2017).

#### 3.2.6. Summary of Sensitivity Studies

These sensitivity studies illustrate the effects of changes in the external forcing, the initial salinity profile, and snow conductivity on the simulated snow and sea ice: (i) A smooth ocean heat flux prevented a precise representation of the sea ice thickness variations; (ii) using ERA-I long-wave flux was reasonable since the observed RV-Lance flux improved the RMSD by only 0.09 °C (in the snow), which is the sensor resolution of the SIMBA; (iii) the ERA-I air temperature has an important bias, and the observed temperature was required to accurately simulate the snow and ice temperature; (iv) the initial ice salinity had a significant and persistent impact on the winter ice temperature, (v) the snow properties strongly impinge on the quality of the simulation and a precise estimation of the snow density is necessary.

For SIMBA_h, a constant snow density of 390 kg/m$^3$ was sufficient to provide a good agreement between the observed and simulated snow and ice temperature evolution.

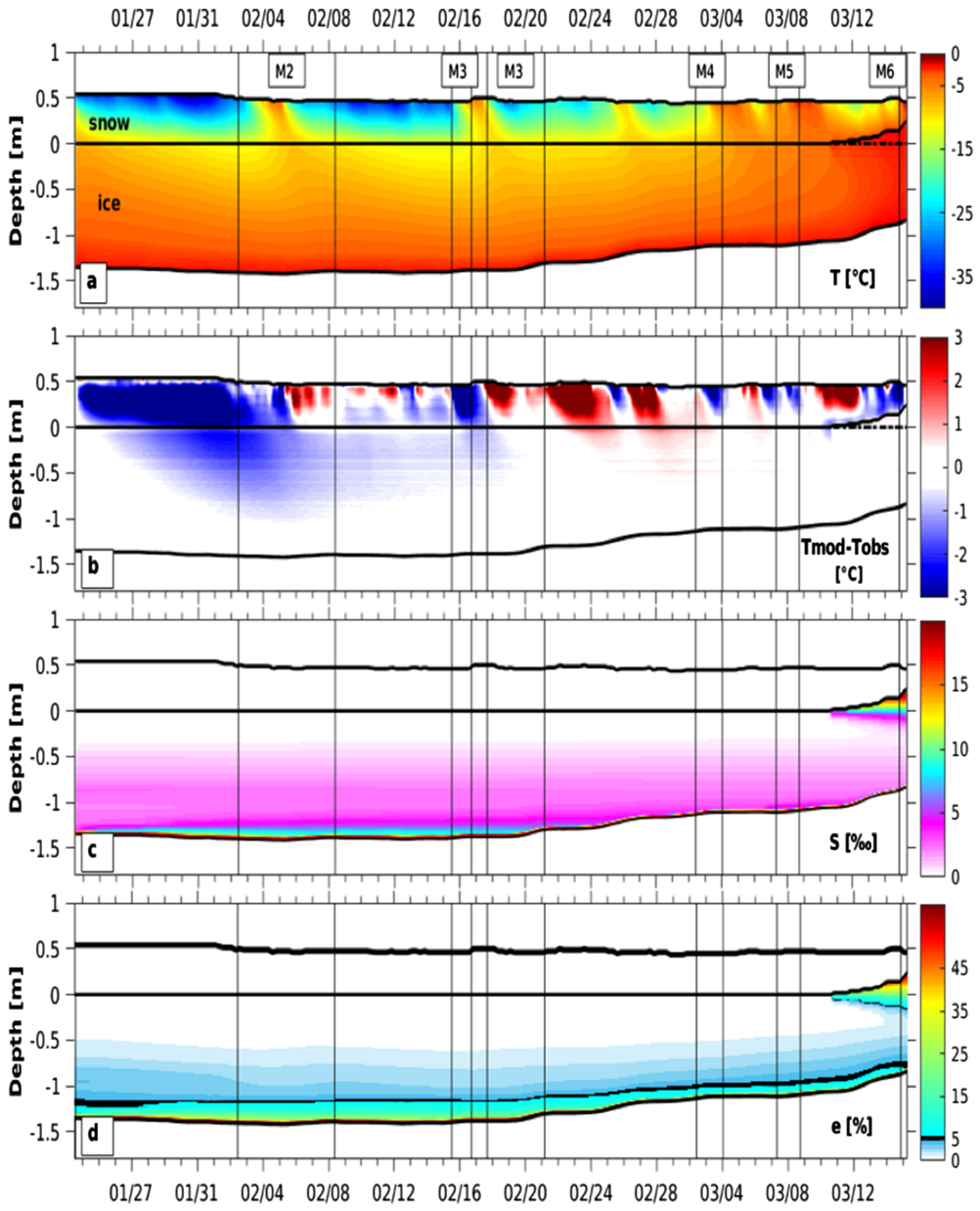


**Figure 8.** Reference run for SIMBA_a. (a) Simulated temperature as a function of time in snow and ice. (b) Temperature differences between simulation and observations. Model outputs are interpolated to the vertical resolution of the data (2 cm). (c) Simulated ice salinity as a function of time. (d) Simulated ice brine fraction as a function of time. The black isoline corresponds to the 5% brine fraction. On all the panels, black lines correspond to the air/snow interface, the lower limit of the snow layer, and ice/ocean interface. Storms are labeled M2, M3, ... , M6 as described in Cohen et al. (2017).

## 4. Simulation Along SIMBA_a Drift

A first simulation of SIMBA_a time series was performed, using the same forcing terms and parameters as for SIMBA_h (in particular, the same snow density of 390 kg/m$^3$) and led to a simulation with a RMSD between the observed and simulated temperature of 2.50 °C in the snow and 0.45 °C in the ice.

### 4.1. Snow Density Adjustment

The two SIMBA buoys featured distinct diffusivity proxy values in the snow with larger values at the SIMBA_a site (1.8 on average) than at SIMBA_h (1.7) (Figures 1d and 1f). As a larger value of the diffusivity proxy is associated with a smaller conductivity and consequently a smaller density, this difference in proxy suggests that the snow density at SIMBA_a was smaller than at SIMBA_h.

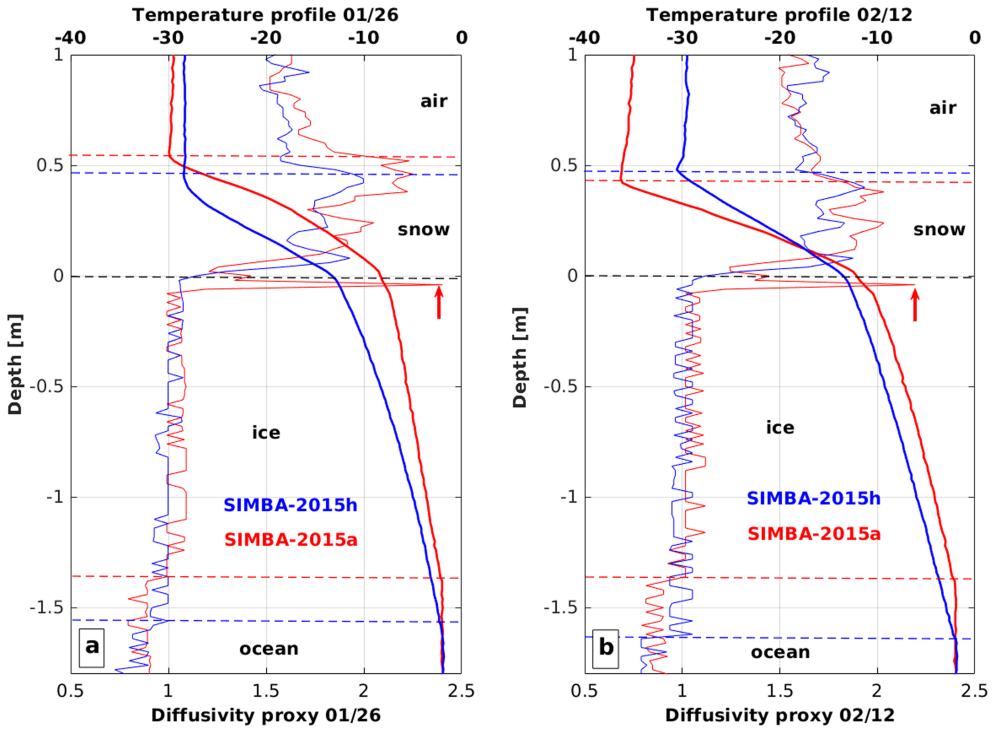


**Figure 9.** Observed diffusivity proxy (thin) and temperature profiles (bold) for SIMBA_h (blue) and SIMBA_a (red) on (a) 26 January and (b) 12 February. The air/snow and ice/ocean interface are represented by dashed lines. Zero is the snow/ice interface. The red arrow points at the anomalous layer (see appendix A).

A simulation with a snow density of 370 kg/m$^3$ (a conductivity of 0.39 W/K/m) reduced the RMSD between the observed and simulated temperature profiles to 2.49 °C in the snow and 0.40 °C in the ice (Figures 8a and 8b). The simulated snow temperature was still 2 to 5 °C colder than the observations during the first ten days (Figure 8b). A closer look at SIMBA_a diffusivity proxy profiles (Figure 9a) showed the existence of two layers of snow with well-differentiated diffusivity proxy values: 2.2 on average in the upper 20 cm of snow and 1.8 in the lower 30 cm. These differences in diffusivity proxy led to a change of slope in the observed snow temperature profile (Figure 9a). The simulated temperature profiles have a constant slope if conductivity and density are the same in the five snow layers (Figure 10b).

We adjusted the snow density of the upper two layers to 240 kg/m$^3$ (corresponding to a snow conductivity of 0.16 W/m/K) until 1 February, to account for the presence of a lighter snow layer that was later blown away at the beginning of storm M2 (Figure 1f). In the lower three layers, we kept a density value of 370 kg/m$^3$ (snow conductivity: 0.39 W/m/K). The simulated snow temperature profiles were much closer to the observations (Figure 10b) with the RMSD dropping from 2.49 to 2.14 °C (Figure 10c).

### 4.2. Simulated Sea Ice

Adjusting the snow density (upper two layers at 240 kg/m$^3$ and lower three layers at 370 kg/m$^3$) improved the simulated ice temperature before 1 February, with a RMSD between observed and simulated ice temperature dropping from 0.40 to 0.35 °C (Figure 10c). Large temperature differences with the measurement located a few centimeters (5 cm) below the snow/ice interface (Figure 10c) occurred in a thin anomalous layer (about 2 cm) with a diffusivity proxy around 2.4, a value much larger than in the ice (1.1; Figures 9 and 1f). This anomalous layer, which persisted until the flooding event (on 10 March), had an insulating effect, partly limiting heat diffusion through the ice (Figures 1f and 9), which led to a thicker simulated ice (Figure 10c). This spurious layer was probably an artifact of the SIMBA_a deployment protocol as explained in the appendix.

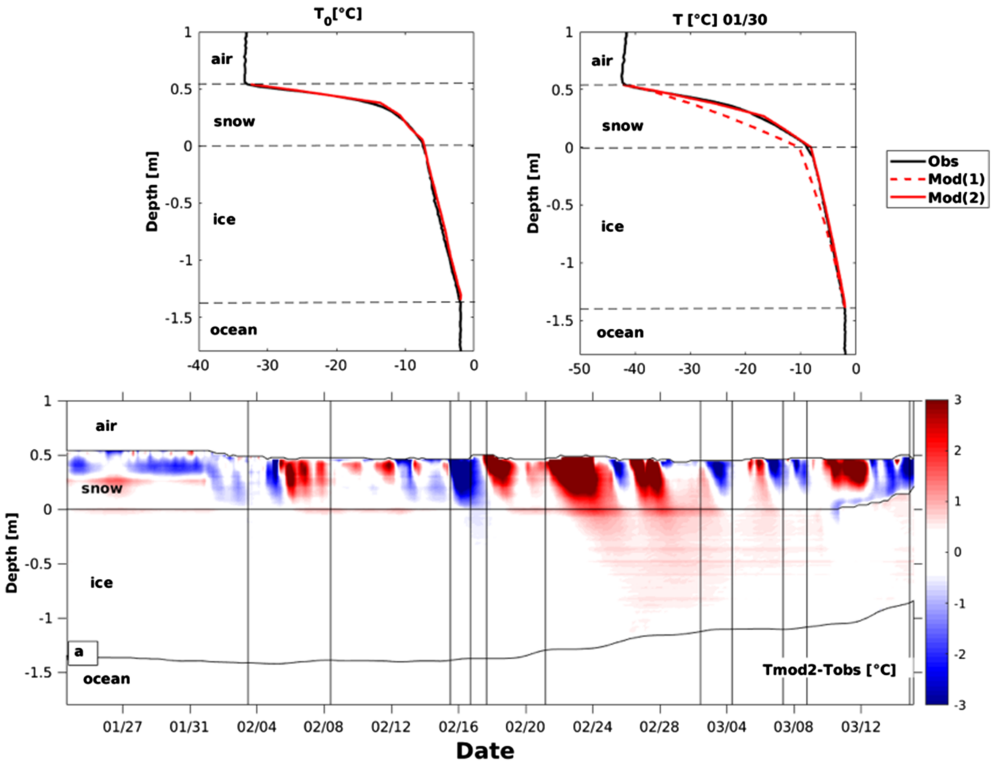


**Figure 10.** (a) Observed (black) and simulated (red) initial temperature profile for SIMBA_a. (b) Observed (black) and simulated temperature profile (mod1: constant snow density is 370 kg/m$^3$; mod2: the snow density of the first two layers is 240 kg/m$^3$ until 1 February). Dashed black lines represent the air/snow, snow/ice, and ice/ocean interfaces. (c) Temperature differences between simulation (mod2) and observations. Model outputs are interpolated to the vertical resolution of the data (2 cm).

## 5. Flooding and Snow Ice Formation

At the end of the record, the heavily snow-loaded floes lost buoyancy due to basal melt. Storm M5 induced the breakup of the floes, and the snow/ice interface sank below the sea level on 8 March for SIMBA_h and 10 March for SIMBA_a (Figure 11). The immersed snow layer was flooded with seawater (around −1.8 °C), inducing a rapid increase of temperature, salinity, and brine fraction (Figures 5 and 8). The mixture of snow and salt water formed a slush layer warmer than the surrounding snow and ice and slowly solidified into snow ice (Provost et al., 2017).

### 5.1. Simulated Temperature in the Slush and Ice During Flooding

Flooding was more gradual at SIMBA_a than at SIMBA_h. A 20 cm thick slush layer was formed in 2 days at SIMBA_h (30 cm at the end of the record, after 7 days) and an only 8 cm thick layer was formed at SIMBA_a (21 cm at the end of the record, after 6 days).

The flooding led to an increase in the observed temperature at the snow/ice interface ($z = 0$) from −5.8 to about −2.4 °C in a few hours for SIMBA_h (Figure 11d) and from −5 to −2.8 °C in two days for SIMBA_a (Figure 11a). The slush layer was slightly colder at SIMBA_a, due to both the more gradual inflow of seawater and the thinner snow layer, which provided less thermal insulation from the cold atmosphere. The heat release associated with the flooding led to a temperature increase of about 3 °C down to 0.50 m in the ice (Figures 11a and 11d).

The simulated temperature in slush and ice was in good agreement with the observations (Figures 11b and 11e). Once the flooding began, the temperature at the snow/ice interface increased from −5.9 to −1.9 °C for SIMBA_h (Figures 11e and 12i; from −4.1 to −2.5 °C for SIMBA_a, Figure 11b). In the two cases, the temperature differences between simulations and observations never exceeded 0.4 °C in the slush layer and underlying ice (Figures 11c and 11f).

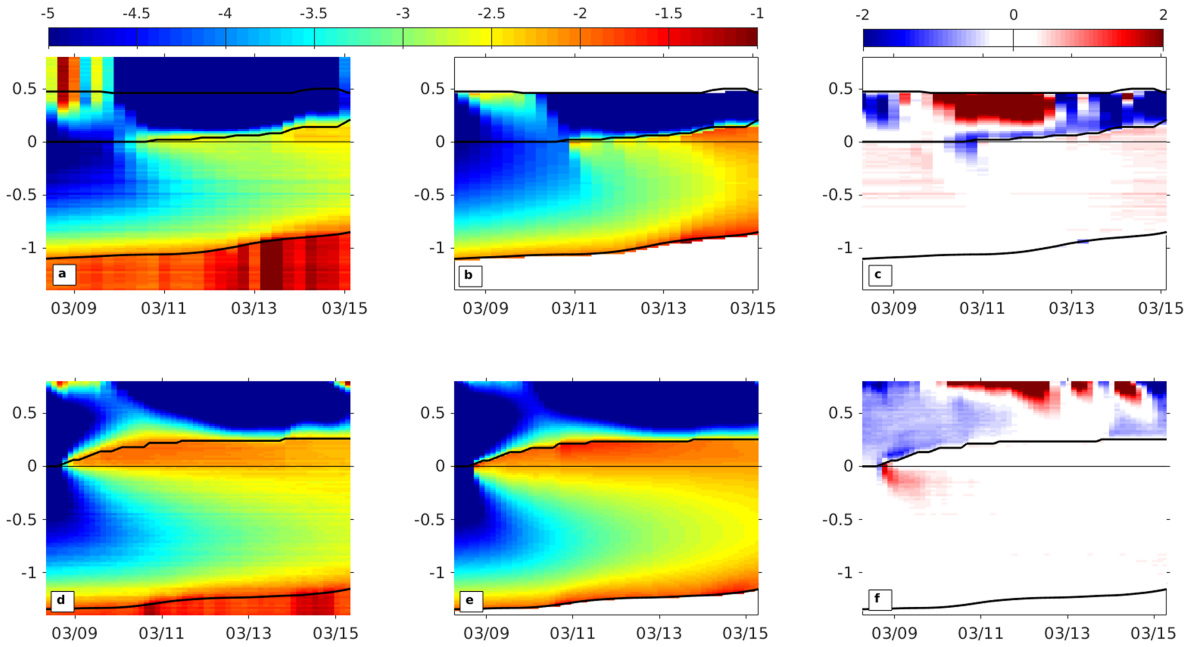


**Figure 11.** (a) Close-up of observed temperature during the period of flooding for SIMBA_a. (b) Close-up of simulated temperature during the period of flooding for SIMBA_a. Outputs have been interpolated to the vertical resolution of the data (2 cm). (c) Temperature differences between simulation and observations for SIMBA_a. (d) Same as (a) for SIMBA_h. (e) Same as (b) for SIMBA_h. (f) Same as (c) for SIMBA_h. Black lines correspond to the air/snow interface, the lower limit of the snow layer, and ice/ocean interface.

### 5.2. Impact of Flooding on Simulated Salinity and Brine Fraction

When seawater invaded the space previously occupied by air in the snow, the simulated salinity increased from 0 to a maximum of 19‰ (Figures 12a and 12d). We now focus on the simulated evolution of salinity, solid fraction, and temperature at SIMBA_h.

Flooding occurred in six steps as the snow/ice interface progressively sank (Figure 12d). At each step, salinity and temperature were maximum at the top of the slush, where additional water ($T > -2$ °C) flooded the overlying snow (Figures 12g and 12i). The solid fraction in the snow was 42% ($\Phi_i = \frac{\rho_{\text{snow}}}{\rho_{\text{ice}}} = 390/917$) before flooding and increased up to 80% at the base of the slush and 55% at the top at the end of the simulation (Figures 12e and 12h). Salinity increased from 0‰ to 8‰ at the base of the slush layer and 17‰ at the top, at the end of the simulation (Figures 12d and 12g).

Below the initial snow/ice interface $z = 0$, the upper ice warming (Figure 12i) led to an increase of porosity down to 40 cm. The solid fraction dropped from 100% to less than 95% in the upper 20 cm (Figure 12h), leading an increase of salinity from 0‰ to 3‰ (Figure 12g).

### 5.3. Snow Ice Formation

Provost et al. (2017) estimated the amount of solidified slush (snow ice) at the end of the record. Assuming that the mass fractions of snow and water in snow ice were 2/3 and 1/3, they found a corresponding snow ice thickness of 8 cm for SIMBA_h and 6 cm for SIMBA_a.

The simulated solid fraction provides the amount of formed snow ice. The initial solid fraction in the slush layer was 42% for SIMBA_h (40% for SIMBA_a). At the end of the simulation, the average of the solid fraction over the slush layer was 60% for SIMBA_h (58% for SIMBA_2015a). The corresponding thickness of the ice fraction in the flooded snow ($h(t)$, gray) and the total ice fraction in the slush layer ($H(t)$, blue) were computed using the following relations (Figures 12c and 12f)

$$h(t) = \Phi_i * h_s(t) \text{ and } H(t) = \frac{S_f(t)}{100} * h_s(t)$$

where $h_s(t)$ is the thickness of the flooded snow and $S_f(t)$ is the average solid fraction of the slush layer

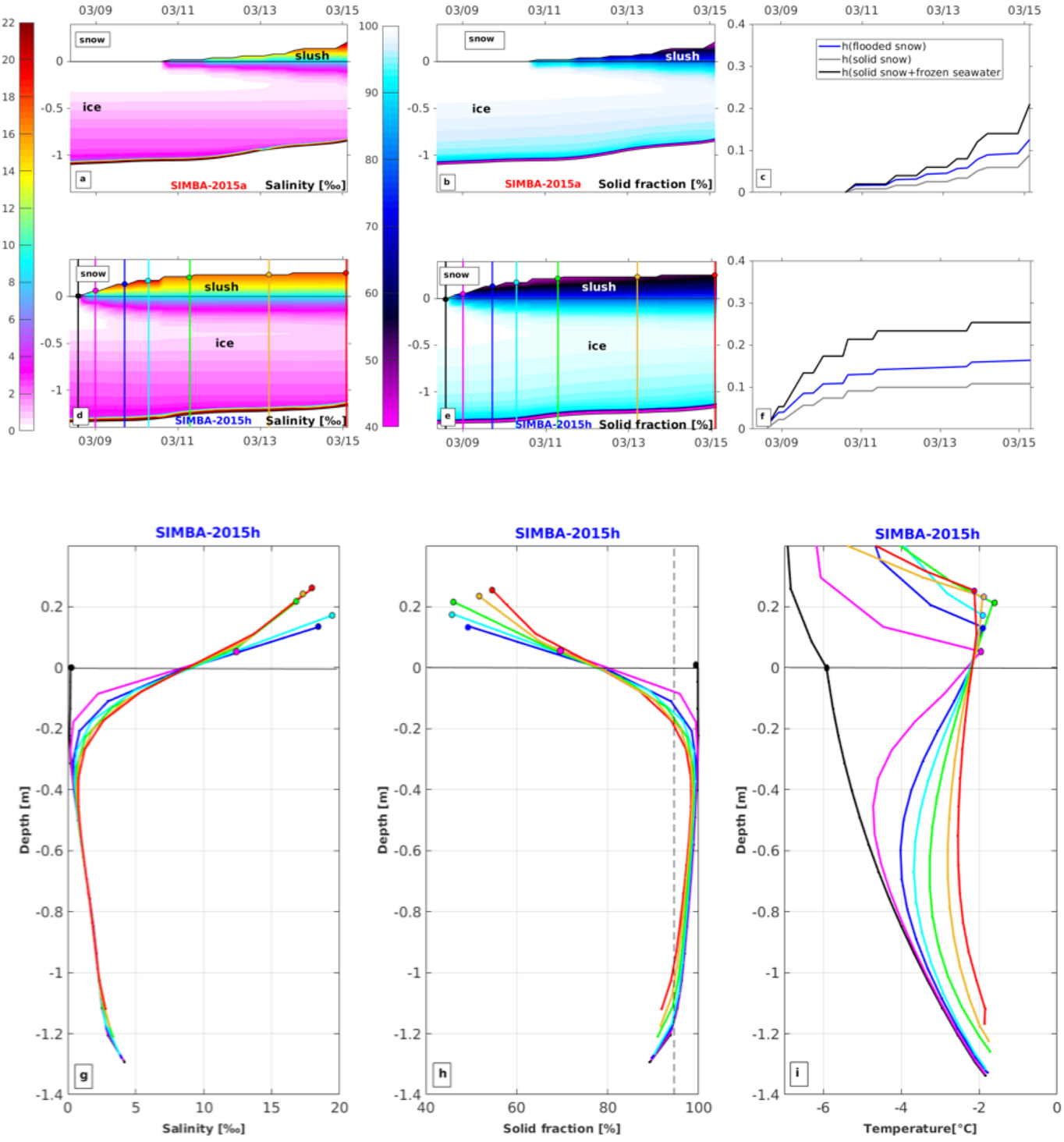


**Figure 12.** (a) Close-up of simulated ice and slush salinity during the period of flooding for SIMBA_a. (b) Close-up of simulated ice and slush solid fraction during the period of flooding for SIMBA_a. (c) Thickness of the flooded snow (black), the solid snow (gray), and the solid snow added to the frozen seawater (blue). (d) Same as (a) for SIMBA_h. (e) Same as (b) for SIMBA_h. The black dot corresponds to the snow/ice interface and colored dots to the snow/slush interface at each step of flooding. (f) Same as (c) for SIMBA_h. (g) Simulated salinity profile at each step of flooding for SIMBA_h. (h) Simulated solid fraction profile at each step of flooding for SIMBA_h (i) Simulated temperature profile at each step of flooding. In panels g, h, and i the initial profile just before flooding is in black, and the color code for the subsequent profiles is the same as in panel d.

(Figure 12h). The estimated amount of formed snow ice, $h_{si}(t) = H(t) - h(t)$, is 5.5 cm at SIMBA_2015h (4 cm at SIMBA_2015a; Figures 12c and 12f). These values are in good agreement with the values obtained by Provost et al. (2017).

## 6. Summary and Perspectives

We revisited the winter SIMBA data provided by the N-ICE2015 campaign, north of Svalbard, using the one-dimensional model LIM1D (Vancoppenolle et al., 2010).

Using five layers of snow instead of one was essential to represent the nonlinear temperature profiles in the snow, in particular during storms when the temperature vertical gradients changed sign. A better representation of the snow temperature profile significantly improves the temperature at the snow ice interface. A multilayer snow system also provided the opportunity to adjust the snow density, since a constant value was not always sufficient to provide a good agreement between the observed and simulated snow and ice temperature profiles.

The reference experiment (SIMBA_h, Figures 5a and 5b) was in good agreement with the observations; the RMSD between observed and simulated temperature profiles was 1.06 °C for the snow and 0.19 °C for the ice. Several sensitivity experiments emphasized the following points: (i) Simulated ice thickness and temperature profiles were not very sensitive to the short timescale (<10 days) variations of the ocean flux; (ii) ERA-I long-wave fluxes were reasonable; (iii) the observed air temperature was necessary because of the warm bias in ERA-I temperature; (iv) a constant initial ice salinity profile of 5‰ (that is typically used in models) introduced an error which was maximum during intense basal melt.

A constant snow density layer is a commonly used simplification. However, snow density varies and is strongly affected by weather conditions (snowfall, wind, and air temperature; e.g., Merkouriadi et al., 2017, Lecomte et al., 2011). Using a constant snow density (390 kg/m$^3$) led to a satisfactory simulation of SIMBA_h temperature profiles evolution and to poor results for SIMBA_a. Even if the two buoys remained within a distance of 20 km, the snow thicknesses and characteristics recorded by the SIMBAs differ significantly. The introduction of a lighter snow in the lower hree3 layers (370 kg/m$^3$) and an even lighter snow in the upper two layers (240 kg/m$^3$ until this lighter snow layer was blown away at the beginning of storm M2) greatly improved the simulation at SIMBA-a. The observed and simulated temperature profiles were jointly used to estimate the snow density (and conductivity). This is a preliminary work, and, in parallel, laboratory studies are ongoing to determine if a (quantitative) relationship between the observed diffusivity proxy and the snow density can be established.

By specifying the observed lower limit of the snow, the flooding episode was simulated and the formation of snow ice quantified. Since the agreement between the observed and simulated temperature profiles was good during the flooding period (temperature difference does not exceed 0.4 °C), the salinity and brine volume computed in the numerical experiment were reliable. The amount of snow ice formed was investigated through the simulated solid fraction. During the flooding event, the simulation led to the formation of approximately 5.5 cm for SIMBA_h (4,0 cm for SIMBA_a). These values are in good agreement with the estimation made by Provost et al. (2017) of 8 cm for SIMBA_h (6 cm for SIMBA_a).

Revisiting winter Arctic ice mass balance observations with a 1-D model validated the interpretations made from the observations (interfaces and ocean heat flux) and provided additional information about the snow (density) and ice (salinity and brine volume). This was useful to more accurately interpret the physical processes at stake in the air/snow/ice/ocean coupled system, such as flooding and snow ice formation. Simulations also pointed out to artefacts due to deployment protocol (see appendix A).

## Appendix: Impact of the Deployment Protocol on SIMBA Observations A

Modeling of SIMBA_a temperature evolution revealed an anomalous value of the diffusivity proxy below the ice-snow interface corresponding to a thin layer with a large insulating effect that impacted temperature evolution (section 4.2). To understand the origin of this thin anomalous layer, we examined the very first stages of refreezing after deployment.

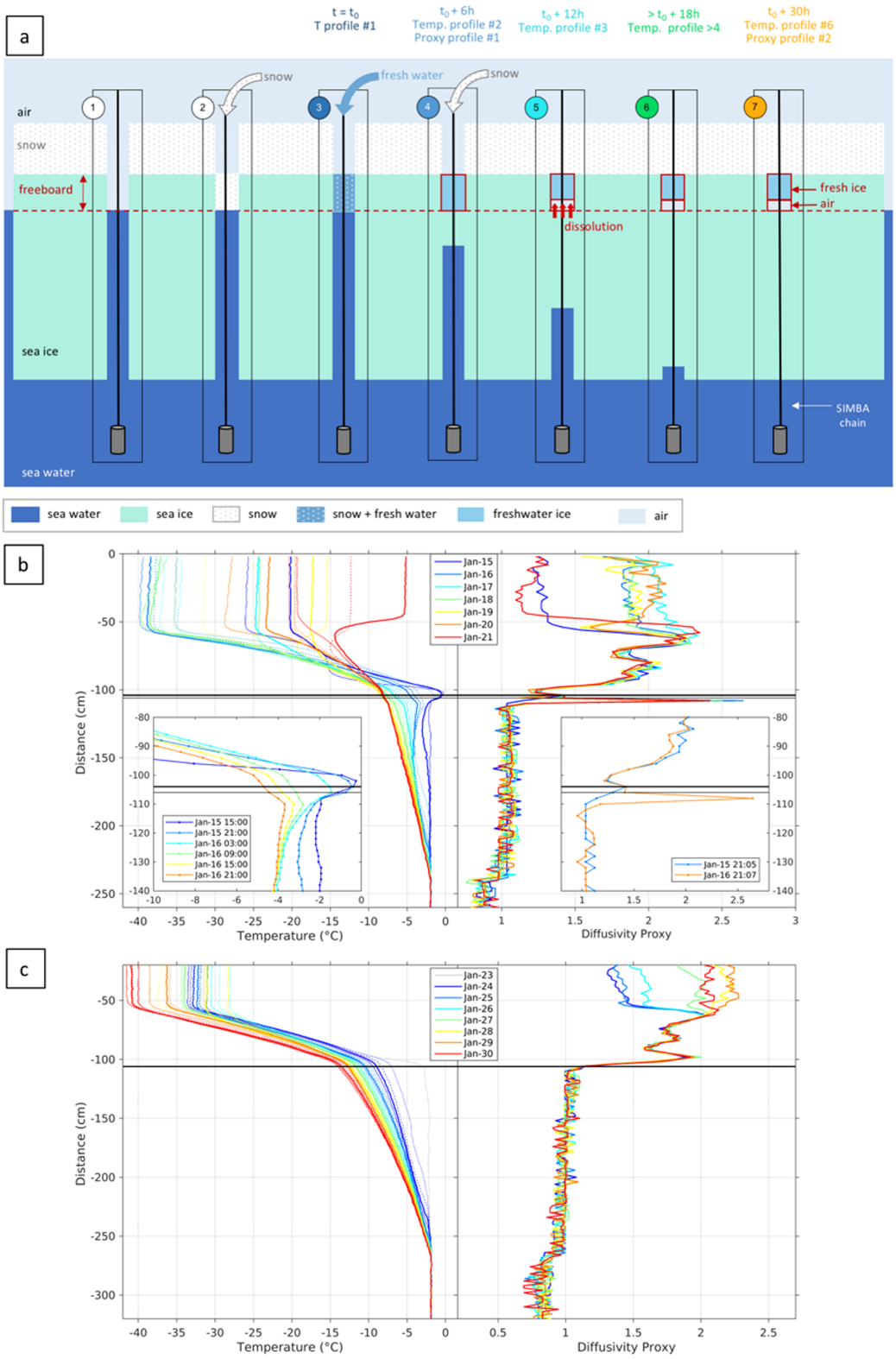


**Figure A1.** (a) Schematics of the deployment protocol for SIMBA_a. (b) Left: First temperature profiles for SIMBA_a (subsampled once a day) during the first week after deployment; insert: close-up of all the temperature profiles near the ice-snow interface (every 6 hr) on the first two days (every 6 hr). Right: First diffusivity proxy profiles for SIMBA_a (during the first week, once a day); insert close up on the proxy profiles near the snow-ice interface during the first two days. (c) Left: First temperature profiles for SIMBA_h (subsampled once a day) during the first week. Right: first diffusivity proxy profiles for SIMBA-h (every 24 hr).

SIMBA-a was deployed on 15 January 2015 during polar night. Air temperature was around −26 °C (Figure 1b). The SIMBA chain was installed at the center of a 5 cm diameter hole through the snow and ice (Figure 1, step 1). A weight maintained the line straight. Once the chain was in place, snow was put above the water to fill the hole up to the snow/ice interface (Figure 1a, step 2) and freshwater was poured over the snow up to the snow/ice interface (Figure 1a, step 3). The mixture of freshwater and snow rapidly solidified into freshwater ice, and snow was added to restore the original snow level (Figure 1a, step 4). The initial temperature profiles from 15 January show values close to 0 °C at a distance of 100 to 108 cm (from the top of the chain), corresponding to the added freshwater. The initial diffusivity profile (15 January) does not show any spurious spike (dark blue profile in Figure 1b). As seawater started to freeze gradually from the top (Figure 1b, light blue profiles), brines were rejected into the water column below and in the freshwater ice above (Figure 1a, step 5). The second diffusivity profile (16 January in orange) shows a spike with values typical of air at a distance of 108 cm. This spike is interpreted as follows: The salt rejected by refreezing seawater may have induced the partial dissolution of the freshwater ice above it, leading to an anomalous layer with air (Figure 1, step 6, 7). The spike in the proxy profile corresponding to this insulating layer, which limited the heat diffusion through the ice, persisted until the flooding event (on 10 March). This interpretation in terms of dissolution of the fresh ice above refreezing seawater results from the absence of a spike in the first proxy profile (6 hr after freshwater was poured) and the emergence and persistence of a huge spike after the second proxy profile (24 hr later; (Figure 1a, step 5).

The temperature profiles at the beginning of the time series provide information on how the different media refroze or behave around the chain (Figure 1b). The seawater in the hole gradually froze from the top to the bottom and was entirely frozen 2 days after the deployment. In 6 hr, 50 cm of seawater has frozen in the hole. The large values of the diffusivity proxy highlight the insulating layer, just below the snow ice interface (Figure 1b).

SIMBA_h was deployed on 23 January 2015. Air temperature was about −33 °C (Figure 1c). The deployment protocol was simpler: Snow was simply added on the refreezing seawater up to the floe snow surface. There was no attempt to restore the ice layer above the 2 cm initial freeboard. Therefore, the measured snow ice interface was at most 2 cm below the unperturbed one. The first temperature profiles showed that more than a meter of water in the hole was refrozen after only 3 hr (Figure 1c). Diffusivity proxy values simply dropped from ice values to snow values at the new snow/ice interface (−2 cm).

**Acknowledgments**
We thank the crew of RV Lance and scientists who participated to the N-ICE 2015 campaign. We acknowledge support from the ANR EQUIPEX IAOOS project, through ANR-10-EQPX-32-01 grant. Parameters from the ERA-Interim reanalysis were obtained from ECMWF. We thank Clément Rousset and Martin Vancoppenolle for helping us with the model LIM1D and constructive discussions. We thank two anonymous reviewers for their comments that helped improve the manuscript. We thank Elisabeth Boles for English proofreading of the manuscript. Sarah Gani benefits from a PhD scholarship from Sorbonne Université, Paris (Ecole Doctorale 129). SIMBA data are available at Sennéchael et al. (2015) https://doi.org/10.17882/59624 and Itkin et al. (2015) https://doi.org/10.21334/npolar.2015.6ed9a8ca and interfaces and ocean fluxes at Sennéchael and Provost (2015) https://doi.org/10.17882/59709.

## References

Andreas, E. L. (1987). A theory for the scalar roughness and the scalar transfer coefficients over snow and sea ice. *Boundary Layer Meteorology*, *38*, 159–184. https://doi.org/10.1007/BF00121562

Bitz, C. M., & Lipscomb, W. H. (1999). An energy conserving thermodynamic model of sea ice. *Journal of Geophysical Research*, *104*, 15,669–15,677. https://doi.org/10.1029/1999JC900100

Cohen, L., Hudson, S. R., Walden, V. P., Graham, R., & Granskog, M. A. (2017). Meteorological conditions in a thinner Arctic sea ice regime from winter to summer during the Norwegian Young Sea Ice expedition (N-ICE2015). *Journal of Geophysical Research: Atmospheres*, *122*, 7235–7259. https://doi.org/10.1002/2016JD026034

Dee, D. P., Uppala, S. M., Simmons, A. J., Berrisford, P., Poli, P., Kobayashi, S., et al. (2011). The ERA-Interim reanalysis: Configuration and performance of the data assimilation system. *Quartely Journal of the Royal Meteorological Society*, *137*(656), 553–597. https://doi.org/10.1002/qj.828

Duarte, P., Meyer, A., Olsen, L. M., Kauko, H. M., Assmy, P., Rösel, A., et al. (2017). Sea ice thermohaline dynamics and biogeochemistry in the Arctic Ocean: Empirical and model results. *Journal of Geophysical Research: Biogeosciences*, *122*, 1632–1654. https://doi.org/10.1002/2016JG003660

Dupont, F., Higginson, S., Bourdallé-Badie, R., Lu, Y., Roy, F., Smith, G. C., et al. (2015). A high-resolution ocean and sea-ice modelling system for the Arctic and North Atlantic Oceans. *Geoscientific Model Development*, *8*, 1577–1594. https://doi.org/10.5194/gmd-8-1577-2015

Golden, K. M., Ackley, S. F., & Lytle, V. I. (1998). The percolation phase transition in sea ice. *Science*, *282*, 2238–2241. https://doi.org/10.1126/science.282.5397.2238

Graham, R. M., Rinke, A., Cohen, L., Hudson, S. R., Walden, V. P., Granskog, M. A., et al. (2016). A comparison of the two Arctic atmospheric winter states observed during N-ICE2015 and SHEBA. *Journal of Geophysical Research: Atmospheres*, *22*, 5716–5737. https://doi.org/10.1002/2016JD025475

Granskog, M., Assmy, P., Gerland, S., Spreen, G., Steen, H., & Smedsrud, L. H. (2016). Arctic research on thin ice—Consequences of Arctic sea ice loss. *Eos, Transactions American Geophysical Union*, *97*(5), 22–26. https://doi.org/10.1029/2016EO044097

Granskog, M. A., Rösel, A., Dodd, P. A., Divine, D., Gerland, S., Martma, T., & Leng, M. J. (2017). Snow contribution to first-year and second-year Arctic sea ice mass balance north of Svalbard. *Journal of Geophysical Research: Oceans*, *122*, 2539–2549. https://doi.org/10.1002/2016JC012398

Hudson, S. and L. Cohen (2016), N-ICE2015 surface meteorology v1. Norwegian Polar Institute (Tromsø, Norway), https://data.npolar.no/dataset/056a61d1-d089-483a-a256-081de4f3308d.

Huwald, H., Tremblay, L.-B., & Blatter, H. (2005). A multilayer sigma-coordinate thermodynamic sea ice model: Validation against Surface Heat Budget of the Arctic Ocean (SHEBA)/Sea Ice Model Intercomparison Project Part 2 (SIMIP2) data. *Journal of Geophysical Research*, *110*, C05010. https://doi.org/10.1029/2004JC002328

Itkin, P., Spreen, G., Cheng, B., Doble, M., Gerland, S., Granskog, M. A., Helgeland, C. (2015). N-ICE2015 buoy data. Norwegian Polar Institute, https://doi.org/10.21334/npolar.2015.6ed9a8ca

Jackson, K., Wilkinson, J., Maksym, T., Meldrum,D., Beckers, J., Haas, C., & McKenzie, D. (2013). A novel and low-cost sea-ice mass balance buoy,*Journal of Atmospheric and OceanicTechnology*, *30*, 2676–2688. https://doi.org/10.1175/JTECH-D-13-00058.1

Jutras, M., Vancoppenolle, M., Lourenço, A., Vivier, F., Carnat, G., & Madec, G. (2016). Thermodynamics of slush and snow–ice formation in the Antarctic sea ice zone. *Deep Sea Research Part II*, *131*, 75–83. https://doi.org/10.1016/j.dsr2.2016.03.008.hal-01303755

Kim, J. G., Hunke, E. C., & Lipscomb, W. L. (2006). A sensitivity analysis and parameter tuning scheme for global sea-ice modeling. *Ocean Modelling.*, *14*, 61–80. https://doi.org/10.1016/j.ocemod.2006.03.003

Koenig, Z., Provost, C., Villacieros-Robineau, N., Sennéchael, N., & Meyer, A. (2016). Winter ocean-ice interactions under thin sea ice observed by IAOOS platforms during N-ICE 2015: Salty surface mixed layer and active basal melt. *Journal of Geophysical Research: Oceans*, *121*, 7898–7916. https://doi.org/10.1002/2016JC012195

Lecomte, O., Fichefet, T., Vancoppenolle, M., & Nicolaus, M. (2011). A new snow thermodynamic scheme for large-scale sea-ice models. *Annals of Glaciology*, *52*(57), 337–346. https://doi.org/10.3189/172756411795931453

Lindsay, R., & Schweiger, A. (2015). Arctic sea ice thickness loss determined using subsurface, aircraft, and satellite observations. *The Cryosphere*, *9*, 269–283. https://doi.org/10.5194/tc-9-269-2015

Maykut, G. A. (1978). Energy exchange over young sea ice in the central Arctic. *Journal of Geophysical Research*, *83*(C7), 3646–3658. https://doi.org/10.1029/JC083iC07p03646

Merkouriadi, I., Gallet, J.-C., Graham, R. M., Liston, G. E., Polashenski, C., Rösel, A., & Gerland, S. (2017). Winter snow conditions on Arctic sea ice north of Svalbard during the Norwegian young sea ICE (N-ICE2015) expedition. *Journal of Geophysical Research: Atmospheres*, *122*, 10,837–10,854. https://doi.org/10.1002/2017JD026753

Overland, J. E., & Wang, M. (2013). When will the summer Arctic be nearly sea ice free? *Geophysical Research Letters*, *40*, 2097–2101. https://doi.org/10.1002/grl.50316

Persson, P., Fairall, C., Andreas, E., Guest, P., & Perovich, D. (2002). Measurements near the Atmospheric Surface Flux Group tower at SHEBA: Near-surface conditions and surface energy budget. *Journal of Geophysical Research*, *107*(C10), 8045. https://doi.org/10.1029/2000JC000705

Pringle, D. J., Eicken, H., Trodahl, H. J., & Backstrom, L. G. E. (2007). Thermal conductivity of Landfast Antarctic and Arctic sea ice. *Journal of Geophysical Research*, *112*, C04017. https://doi.org/10.1029/2006JC003641

Provost, C., Sennéchael, N., Miguet, J., Itkin, P., Rösel, A., Koenig, Z., et al. (2017). Observations of flooding and snow ice formation in a thinner Arctic sea ice regime during the N-ICE2015 campaign: Influence of basal ice melt and storms. *Journal of Geophysical Research: Oceans*, *122*, 7115–7134. https://doi.org/10.1002/2016JC012011

Schmidt, G. A., Bitz, C. M., Mikolajewicz, U., & Tremblay, L.-B. (2004). Ice-ocean boundary conditions for coupled models. *Ocean Model*, *7*, 59–74. https://doi.org/10.1016/S1463-5003(03)00030-1

Sennéchael N., Provost C. (2015), Interfaces and ocean heat flux derived from SIMBA_2015a and SIMBA_2015f data during N-ICE campaign in winter 2015. SEANOE. https://doi.org/10.17882/59709

Sennéchael N., Provost C., Villacieros-Robineau N., Calzas M., Guillot A., Savy J.-P., et al. (2015), IAOOS winter SIMBA data during N-ICE 2015 North of Svalbard. SEANOE. https://doi.org/10.17882/59624.

Spreen, G., Kwok, R., & Menemenlis, D. (2011). Trends in Arctic sea ice drift and role of wind forcing: 1992-2009. *Geophysical Research Letters*, *38*, L19501. https://doi.org/10.1029/2011GL048970

Sturm, M., Holmgren, J., König, M., & Morris, K. (1997). The thermal conductivity of seasonal snow. *Journal of Glaciology*, *43*(143), 26–41. https://doi.org/10.3189/S0022143000002781

Urrego-Blanco, J. R., Hunke, E. C., & Urban, N. (2016). Uncertainty quantification and global sensitivity analysis of the Los Alamos sea ice model. *Journal of Geophysical Research: Oceans*, *112*, 2709–2732. https://doi.org/10.1002/2015JC011558

Vancoppenolle, M., Fichefet, T., & Goosse, H. (2008). Simulating the mass balance and salinity of Arctic and Antarctic sea ice. 2: Importance of sea ice salinity variations. *Ocean Modelling*, *27*(1-2), 54–69. https://doi.org/10.1016/j.ocemod.2008.11.003

Vancoppenolle, M., Goosse, H., de Montety, A., Fichefet, T., Tremblay, B., & Tison, J.-L. (2010). Modeling brine and nutrient dynamics in Antarctic sea ice: The case of dissolved silica. *Journal of Geophysical Research*, *115*, C02005. https://doi.org/10.1029/2009JC005369

Vancoppenolle, M., & Tedesco, L. (2017). *An introduction to sea ice, chap. 20 Numerical models of sea ice biogeochemistry*, (pp. 492–515). Wiley. https://lccn.loc.gov/2016031586

Vihma, T., Pirazzini, R., Fer, I., Renfrew, I. A., Sedlar, J., Tjernström, M., et al. (2014). Advances in understanding and parameterization of small-scale physical processes in the marine Arctic climate system: A review. *Atmospheric Chemistry and Physics*, *14*, 9403–9450. https://doi.org/10.5194/acp-14-9403-2014

Zhang, J., & Rothrock, D. A. (2001). A thickness and enthalpy distribution sea-ice model. *Journal of Physical Oceanography*, *31*, 2986–3001. https://doi.org/10.1175/1520-0485(2001)031<2986:ATAEDS>2.0.CO;2